Chinese Chemical Letters 34 (2023) 107304

Contents lists available at ScienceDirect

Chinese Chemical Letters

journal homepage: www.elsevier.com/locate/cclet

Trapping precursor-level functionalities in hierarchically porous carbons prepared by a pre-stabilization route for superior supercapacitors

Mulati Mansuer[a,1], Ling Miao[a,1], Yang Qin[a], Ziyang Song[a], Dazhang Zhu[a], Hui Duan[a], Yaokang Lv[c], Liangchun Li[a], Mingxian Liu[a,b,*], Lihua Gan[a,*]

[a] Shanghai Key Lab of Chemical Assessment and Sustainability, School of Chemical Science and Engineering, Tongji University, Shanghai 200092, China
[b] College of Chemistry and Molecular Engineering, Zhengzhou University, Zhengzhou 450001, China
[c] College of Chemical Engineering, Zhejiang University of Technology, Hangzhou 310014, China

ARTICLE INFO

Article history:
Received 2 January 2022
Revised 26 February 2022
Accepted 7 March 2022
Available online 9 March 2022

Keywords:
Carbon-based supercapacitors
Quinone-amine network
Pre-stabilization process
Symmetric device
Polymer electrolyte

ABSTRACT

Versatile module design of precursor networks enables flexible functionalization of nano-carbon electrode materials to meet the adaptable energy-storage demand. Functionalized heterogeneous networks are more likely to decompose by swift temperature programming together with predesign module removal, so high functionality/network transfer from precursor to carbon is still a work in progress. A pre-stabilization route is proposed here to enhance the network strength at early pyrolysis and pin up precursor-level functionalities on the final carbon. Such strategy successfully fixes more electroactive N (4.28−8.86 wt%) into the resultant carbon microspheres compared with non-pretreated carbon (2.89 wt%), as well as achieves broad ion-accessible platforms of 1575–2269 m^2/g with preset structural superiorities. As a result, a typical acidic device reveals an outstanding specific capacitance of 383 F/g at 10 mV/s. Taking advantage of a novel $LiNO_3$-PAM polymer electrolyte, the upgraded symmetric device displays the maximum specific capacitance of 229 F/g, along with a boosted energy density of 41.1 Wh/kg at 643.4 W/kg. This work opens up a feasible insight into realizing highly efficient precursor/electrode design toward superior system with outstanding energy/power feature and temperature applicability.

Supercapacitor is a type of innovative energy storage devices with extraordinary performances for combining the advantages of traditional capacitors and batteries [1–4]. One of the most important components for charge storage in supercapacitors is electrode materials, so development of new/practical electrode materials is critical to the research and application of supercapacitors [5–7]. According to recent reports on electrode materials, porous carbon spheres manifest specific merits for electrode materials by achieving high packing density and regular porosity compared to other carbon materials [8,9]. For instance, Feng *et al.* proposed a pomegranate-like carbon microspheres for high-efficiency EDLCs with a high specific capacitance of 254 F/cm^3 at 1 A/g [10]. More recently, Du *et al.* designed yolk–shell carbon-sphere electrodes with tunable structures, of which specific capacitance reached 330 F/g at 0.5 A/g [11].

The unique pyrolysis design for organic salt/polymer precursors (*e.g.*, metal complexes, conjugated polymer networks, ionic liquids) enables high levels of functional groups to be introduced into the carbon scaffold [12,13]. B–C bond improves the rigidity of the polymer backbone as well as offers a densely electroactive surface [14]. Carbonyl group (C=O) can bring rapid electron transfer kinetics during the charge/discharge process, which reveals strong redox reactivity [15,16]. Unfortunately, the low overall thermal stability of most organic compounds results in decomposition into volatile vapors during the pyrolysis process, thereby losing their elaborately designed precursor-level functionalities [17,18]. The design of synthetic precursors with ideal chemical structures and corresponding protection measures of the carbon architectures is still a work in progress.

Desirable EDLC is greatly attributed to high surface areas and suitable pore size distributions for carbon materials [19,20]. In the process of activation, implementing etching agents such as alkali metal compounds (*e.g.*, LiOH, KOH, NaOH, $KHCO_3$ and $KMnO_4$) can produce large specific surface area and rich porosity [21–23]. Due to the fact that organic substances tend to be decomposed in alka-

* Corresponding authors.
E-mail addresses: liumx@tongji.edu.cn (M. Liu), ganlh@tongji.edu.cn (L. Gan).
[1] These authors contributed equally to this work.

https://doi.org/10.1016/j.cclet.2022.03.027
1001-8417/

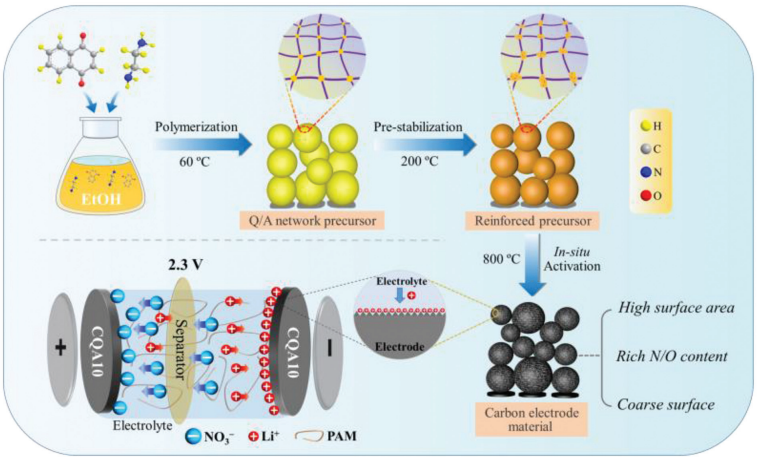

Fig. 1. Schematic diagram for the preparation of carbon microspheres by pre-stabilization route, and illustration of the polymer electrolyte based device configuration with charge-storage mechanism.

line media at high temperature, the strong activation process will inevitably result in morphological defects and poor heteroatom surface carbons [24]. To conquer this, Tian *et al.* proved a molten salt to exhibit insignificant destructive influence on the inherent structure of rice husk precursor as an activator [25]. Benefiting from the redox-reaction etching nature of $CuCl_2$, the rice husk carbon possess combined merits of high surface area and improved heteroatom content. However, altering the etching agent is still difficult to simultaneously realize functionalized heteroatoms and the rigidity of the carbon skeleton during the high temperature treatment [26–28].

Herein, carbon microspheres with tailored structures, high surface area and controllable *in-situ* heteroatom doping are achieved based on a straightforward coupling strategy between model quinone and amine. Thanks to the appropriate pre-stabilization route utilized, the electroactive N content is significantly improved comparing with non-pretreated carbon, as well as realizes excellent specific surface area and high carbon residue rate without sacrificing the external morphology. Owing to regular spherical appearance and high-level fluidity, the typical electrode material displays excellent adaptability to electrolytes. A typical acidic device manifests an excellent specific capacitance of 383 F/g at 10 mV/s. Extending the voltage window to 2.3 V with $LiNO_3$-PAM polymer electrolyte endowing the symmetric device with a high energy density of 41.1 Wh/kg at 643.4 W/kg.

The systematic preparation of polymeric quinone-amine (PQA) employing naphthoquinone (Q) and ethylenediamine (A) as a model quinone/amine pair is shown in the Fig. 1, followed by a schematic diagram of the 2.3 V device configuration and charge-storage mechanism composed of the typical electrode material. It is known that Q can be covalently coupled to A through Michael addition and/or Schiff base reactions [17]. For this purpose, the electrospray ionization-mass spectrum (ESI-MS) of the PQA solution is recorded 10 min after the reactants are combined. Among the most probable molecular structures, the one depicted with red represents the largest amount of the products (III, relative abundance $\geq$ 80%), which is performed by Michael-addition polymerization reaction while the abundance of Schiff base products is about 15% (I, Fig 2a) [29,30]. According to the comparison of the characteristic absorption peaks, FT-IR analysis is utilized to evaluate the states of related groups caused by temperature changes. Fig. 2b depicts the FT-IR spectra for the PQA polymers under different pre-stabilized times. The adsorption peaks at 746 and 1305 cm^{-1} can be attributed to the blending vibration of –NH– groups and the stretching vibration of C–N groups which indicate the occurrence of the Michael addition reaction [31]. The corresponding stretching vibration of N–H appears at 3342 cm^{-1} for proving the existence of a secondary amine. In addition, the characteristic peak of C=N bonds appear at 1602 cm^{-1}, which implies the formation of Schiff base polymers [32]. It is worth mentioning that the C=O appears at the standard position of 1688 cm^{-1}, and then the peak intensity of C=O remains at a high level as the growth of pre-stabilization time, indicating that the pre-stabilization route can effectively avoid the decomposition of highly electroactive carbonyl group [33].

The weight loss during pyrolysis can be revealed to a certain extent by the thermogravimetric (TG) retention. Therefore, TG test is investigated for the carbon yields of the PQA precursors which undergone different pre-stabilization times (Fig. 2c). It can be discovered that the pre-stabilized samples achieve almost zero weight loss before ~300 °C because of the protection path due to pre-stabilization in the early stage. Generally, the samples experienced pre-stabilization treatment at a constant temperature of 200 °C for 2 h show significantly improved carbon residual rates by 64.6% (PQA05), 73.1% (PQA10) and 72.5% (PQA20). However, the sample without pre-stabilization (PQA) exhibits only 53.9% of sample yield (Fig. 2d). During the pre-stabilization process (gray pillar in Fig. 2d), at the beginning of the period from 0 to 5 h (PQA–PQA05), due to the desorption of polymer adsorbed water, there is a significant weight loss reducing from 100% to 92.8%, and then the residual yield increases (92.8%–93.8%) with the growth of the stabilization time from 5 h to 20 h (PQA05–PQA20), indicating the complete reinforcement of the carbon skeleton [33]. After further activation of the pre-stabilized products (orange pillar in Fig. 2d), the yields of the final carbon material to the initial precursor is 59.9% (PQA05), 68.3% (PQA10), 68.0% (PQA20) respectively, proving the pre-stabilization can suppress the continues loss of the precursor by increasing the sample yield by up to 26.7% [34]. However, excessive pre-stabilization process will not improve the precursor yield but intensify the corresponding energy consumption, indicating that the appropriate pre-stabilization time should be 10 h. XRD patterns of the carbonized quinone-amines (CQA*x*) exhibit similar wide diffraction peaks located at 28° and 41°, indicate the amorphous structure of carbons according to the (002) and (100) diffractions (Fig. S1a in Supporting information) [35]. Raman spectrum further identifies the structural features of four samples (Fig. S1b in Supporting information), exhibiting two pronounced peaks at 1345 cm^{-1} (D-band, disordered phase) and 1589 cm^{-1} (G-band, graphitic phase) [36]. As the duration of the treatment alters from 0 to 20 h, the I_D/I_G value drops from 0.94 to 0.89, revealing the

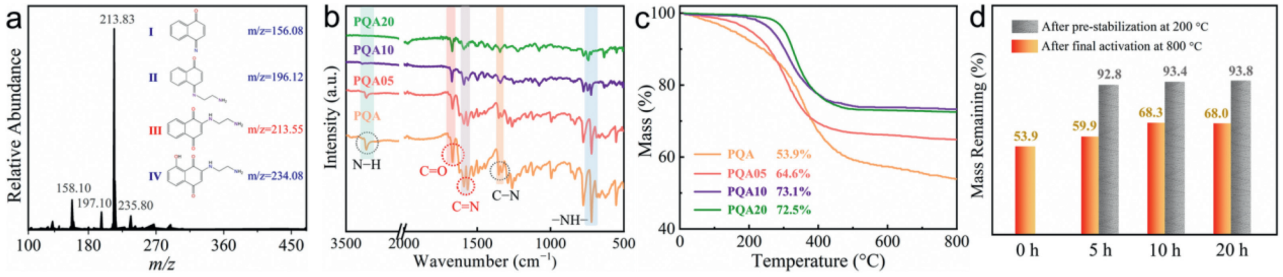

Fig. 2. (a) ESI-MS spectrum of the solution after 10 min of reaction (the inset shows only one possible regioisomer). (b) FT-IR spectrum of the PQA*x* with temperature variation. (c) TGA curves. (d) Mass remaining of precursor after pre-stabilization and carbonization separately.

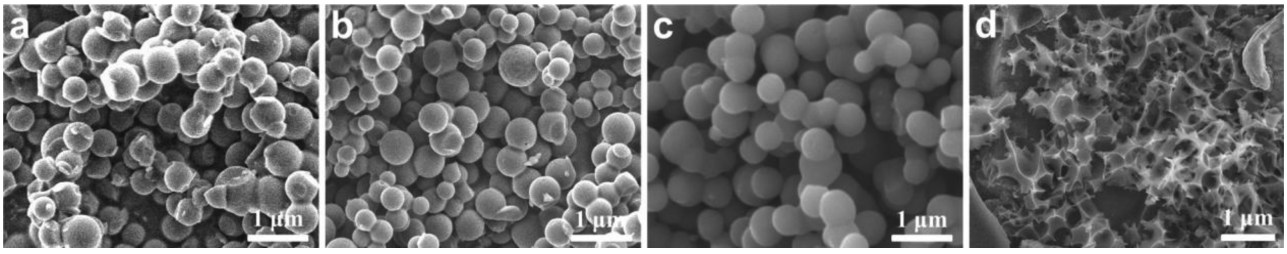

Fig. 3. SEM images of (a) CQA05, (b) CQA10, (c) CQA20 and (d) CQA.

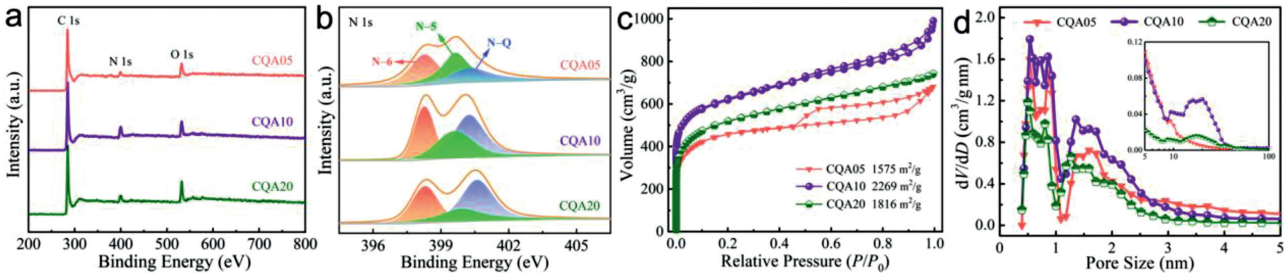

Fig. 4. (a) XPS wide-scan spectra of CQA*x* and (b) high-resolution spectra of N 1s. (c) N_2 adsorption-desorption isotherms and (d) pore size distributions of CQA*x*.

pre-stabilization boosts the quantity of graphitic micro-domains [24].

SEM micrographs reveal the overall morphology and structure of the pyrolyzed carbon products. Pre-stabilized products manifest a micro-spherical shape with a diameter of 330∼660 nm, probably due to the formation of emulsion droplets in ethylenediamine-ethanol solution, which is favorable to obtain spherical morphology (Figs. 3a–c). Observably, pre-stabilized carbons (CQA05–CQA20) significantly maintain the complete microsphere morphology. Among them, CQA05 reveals partially collapsed and overlapped morphology while CQA reflects that the carbon skeleton is substantially destroyed by overheating and KOH etching (Figs. 3a and d) [37]. Exceeding 10 h of pre-stabilization keeps the microspherical appearance basically remains at a high level (Figs. 3b and c). However, the surface of CQA20 is too smooth to expose enough electrochemically active sites while CQA10 owns coarse surface to absorb abundant electrolyte ions. In contrast, CQA shows a flaky morphology due to the intense etching effect of potassium hydroxide (Fig. 3d). EDS diagrams of CQA10 illustrate the uniform dispersion of N/O on the carbon surface (Fig. S2 in Supporting information) [33]. TEM images of CQA10 further prove that there are a large number of hierarchical pores in the carbon framework, which can be attributed to the *in-situ* activation process (Fig. S3 in Supporting information).

The full XPS spectrum of CQA*x* provides three absolute peaks positioned at 284.9 (C 1s), 399.6 (N 1s) and 533.4 (O 1s) eV (Fig. 4a and Fig. S4a in Supporting information), demonstrating the successfully co-doping of N and O elements. Owing to the suitable pre-stabilization route, the carbons (CQA05–CQA20) possess significantly increased nitrogen content of 4.28–8.86 wt%, while CQA shows very limited nitrogen content of 2.89 wt% (Table 1). Therefore, a crucial excellency of the pre-stabilization is the capability of allowing high-degree nitrogen doping into the fully-developed porous carbon architecture. XPS test also investigates the chemical state of the particular elements. There are three distinct peaks in the C 1s spectra, indicating the existence of C-1 (C=C, 284.2 eV), C-2 (C−N/C−O, 286.3 eV) and C-3 (C=N, 288.7 eV) (Figs. S5a−d in Supporting information) [28], revealing the quinone-amine network derived carbons. The N doping forms in the carbon framework are as follows, containing N-6 (pyridinic N, 398.2 eV), N-5 (pyrrolic N, 399.5 eV) and N-Q (quaternary N, 400.6 eV), respectively (Fig. 4b and Fig. S4b in Supporting information) [38]. Among them, N-6 and N-5 have roles as electron donors and the main nitrogen-containing functional groups for providing rich electrochemical active sites to produce pseudocapacitance. N-Q enhances electronic conductivity of carbon materials, which can lower the charge transfer resistance during charge/discharge process [39].

Table 1
Total sample yield and element compositions of CQA*x*.

Samples	Yield (%)	C (wt%)	N (wt%)	O (wt%)
CQA05	59.9	85.03	4.28	10.69
CQA10	68.3	79.03	8.86	12.11
CQA20	68.0	76.52	4.67	18.81
CQA	53.9	86.51	2.89	10.60

High-resolution O 1s spectra of CQA*x* can be deconvoluted into three different component peaks, focusing on O-1 (C=O, 530.8 eV), O-2 (C−OH, 532.2 eV) and O-3 (O=C−O, 533.7 eV) can be differentiated in Figs. S5e−h (Supporting information). The functional groups of C/O, such as C-3 (C=N) and O-1 (C=O), impart the carbon matrix with high stability, affinity and hetero-atomic chemical transfer process to realize efficient energy storage [6]. Compared with commercial activated carbon (129°), the water contact angles of CQA*x* are much smaller (47°−81°), which have the connection with the total heteroatom content by enhancing the pore accessibility of electrolyte ions enter and immerse into the internal active surface (Fig. S6 in Supporting information) [40]. It turns out that pre-stabilization has a significant improvement in N/O atom retention as well as sample yield compared to the state-of-the-art activation techniques (Table S1 in Supporting information).

The nitrogen adsorption-desorption isotherms of pre-stabilized carbons are shown in Fig. 4c. CQA*x* exhibit a sharp increase in adsorption volume when $P/P_0 < 0.05$, demonstrating the existence of abundant micropores. The hysteresis loops at $P/P_0 = 0.45{\sim}0.9$ and the sharp rise at $P/P_0 = 0.95{\sim}1.0$ indicate the presence of the meso– and macropores in CQA*x*, revealing the hierarchical porous structures of CQA*x* [38]. In general, the carbons exhibit extra-high surface areas of 1575 m^2/g for CQA05, 2269 m^2/g for CQA10 and 1816 m^2/g for CQA20, due to the robust route for both synthesis and pre-stabilization treatment. Along with increased degree of pre-stabilization, the specific surface areas of the carbons show a trend of gradually increase and then to decrease. Among the samples from CQA05 to CQA20, the micropores of carbons are mainly concentrated at 0.55, 0.88 and 1.3 nm, accompanied by abundant meso– and macropores. In contrast with CQA05, CQA10 owns higher amounts of pores peaked at 0.55, 0.88 and 1.3 nm. Pre-stabilization process exhibits immediate effects on the numbers of corresponding pores in each position, which does not generate unnecessary pore expansion effect (Fig. 4d). The micro- and mesopores of carbons are produced by the gradual release of thermally unstable fragments, which provide enough active sites for ion adsorption and quick ion migration [41]. As seen from Fig. 4d inset, CQA10 contains a certain amount of large pores as ion-storage sites in specific intervals which may be originated from the carbon oxide gas produced by alkali etching of carbon in the late carbonization period [42].

To verify the effectiveness of the route and variables on pre-stabilization of carbon materials, the electrochemical performances of CQA*x* are evaluated by symmetrical device (0−1 V) using classic alkaline/acid electrolytes (refer KOH and H_2SO_4). Figs. S7a and b (Supporting information) show typical rectangular shaped CV curves and triangle GCD curves without distortion that conform the capacitance response mainly stem from the formation of electric double layer in KOH electrolyte. By the integration of the CV curves, the gravimetric capacitances in KOH at 10 mV/s are 318 F/g for CQA05, 365 F/g for CQA10, 338 F/g for CQA20 and 299 F/g for CQA, respectively (Fig. S7a). As shown in Fig. S7c (Supporting information), Nyquist diagrams are composed of almost vertical lines in the low frequency region and semicircular parts in the high/mid frequency region. By fitting the equivalent series circuit of this special graph, the intersection of the semicircle and the *X* axis can reflect the equivalent series resistance (R_s), and the radius of the semicircle can be indexed to the charge transfer resistance (R_{ct}) [43]. CQA*x* electrodes exhibit favorable R_s values within the range of 0.48–0.82 Ω, and R_c values ranging from 0.26 Ω to 0.41 Ω. Among electrodes, CQA10 exhibits low-capacity attenuation under various scanning rates and current densities, indicating superb rate performance (Figs. S7d–f in Supporting information). For investigating the redox mechanism of quinone/amine in acidic medium and its influence on the total capacitance behavior, the electrochemical measurement with H_2SO_4 electrolyte is also carried out. The CV curves of the H_2SO_4 based supercapacitors show *quasi*-rectangular shapes with pairs of clearly widened humps at ∼0.6 V (Fig. 5a), which implies the collaborative operation of EDLC and the Faradaic reactions of the N/O active parts. By the integration of the CV curves, the specific capacitance of CQA10 at 10 mV/s is 383 F/g, higher than the values of counterparts, followed by 325 F/g (CQA05), 342 F/g (CQA20) and 301 F/g (CQA). The GCD curves also depict triangular shapes with obvious curvature at ∼0.6 V, of which CQA10 shows relatively stronger distortion due to higher level heteroatom-induced Faradaic reactions at the carbon interface (Fig. S8a in Supporting information). In this attempt, it is worth mentioning that the specific capacitances of CQA*x* generally higher than that of the KOH supercapacitors which can be attributed to the quinone/hydroquinone switching and pyridinic/pyrrolic nitrogen responses (Figs. S8a–c in Supporting information). The comparison chart of the six parameters for CQA*x* samples indicates that a large specific surface area and developed porosity along with abundant Faradaic active sites can initiate a higher capacitive performance (Fig. S9 in Supporting information) [44]. Upon cycling, KOH/H_2SO_4 based devices reveal excellent capacitive endurances (96.8%/93.8% energy retention at 1 A/g after 20,000 cycles) with 97.2%/95.4% retaining columbic efficiencies (Figs. S7g and S8h in Supporting information).

For evaluating ion/electron transport kinetics of CQA*x* electrode in H_2SO_4 electrolyte, the capacitive behavior of device is investigated by CV test data according to the relationship of $i = av^b$ (*i*, current density; *v*, scan rate) (Fig. 5b) [39,45]. The *b* value is a key indicator for evaluating charge storage kinetics, of which close to 1 indicates ideal EDLC behavior and ultrafast charge storage kinetics. By plotting log*i* and log*v* (the scan rate range is 10−200 mV/s), the slope of the *b* value as the cathode/anode fitting line is 0.94 and 0.93, manifesting almost ideal charging storage dynamics in H_2SO_4 electrode. Simultaneously, by decoupling the capacitances form fast-kinetic processes (electric double layer capacitance) and slow-kinetic processes (pseudocapacitance), the ion/electron transport kinetics effectiveness of capacitive behavior is quantitatively compared referring to equation $i = a_1v + a_2v^{0.5}$ (Fig. 5c and Fig. S10 in Supporting information) [46]. When the typical device is switched to utilize H_2SO_4 electrolyte instead of KOH electrolyte, the slow-kinetic ratio significantly improves from 3.2%–21.3% to 4.8%–24.3%, elucidating that the pseudocapacitance effect of N/O groups in acidic electrolytes is stronger than that in alkaline electrolytes (Fig. 5d). The remarkable capacitance of 383 F/g at 10 mV/s attributing to the combination of reasonable pore size distribution, proper amount of heteroatom doping and stable engineered structure. CQA10 exhibits the minimum R_s value (0.29 Ω) and R_{ct} value (1.02 Ω), are lower than counterparts owing to its higher electrochemical reactivity and ion accessibility (Fig. S8d in Supporting information) [47]. The Bode plots further reveals the representative frequency *f*, which corresponds to the semi-infinite Warburg impedance of the fast transition of electron transport dynamics, and can intuitively reflect the relaxation time constant τ (= 1/*f*). The τ value of CQA10 is 1.43 s, which is smaller than the corresponding value of τ (2.48– 3.98 s), implying a fast frequency response by multi-scale pore network for endowing fast energy storage/transmission functions (Fig. S8e in Supporting information) [48]. In addition, it is necessary to quarry the diffusion resistance σ which extracted quantitatively from the slope of the fitted line for evaluating electrolyte ion diffusion kinetics (Fig. S8f in Supporting information). The σ value of CQA10 is also the smallest (0.50 $\Omega\ s^{-0.5}$), indicating the critical influence of carbon-surface modification and multi-dimensional framework construction on ion diffusion and accelerated electrolyte penetration (Table S2 in Supporting information) [45].

In recent years, the development of supercapacitors based on polymer electrolytes has made significant progress in order to

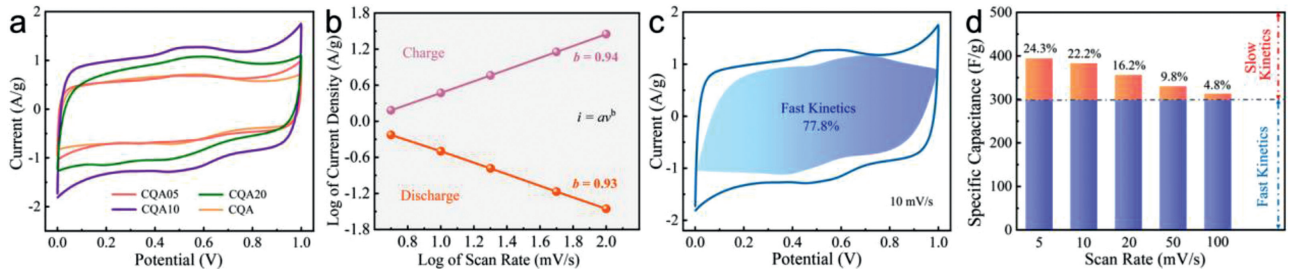

Fig. 5. Electrochemical behaviors of the symmetric supercapacitors based on CQA*x* electrodes using H_2SO_4 electrolyte: (a) CV curves at 10 mV/s. (b) Relationship between absolute scan rate and current density obey the power law of CQA10. (c) The decoupling of the capacitance from slow-kinetics and fast-kinetics processes of CQA10. (d) Distribution histogram of capacitance contribution of CQA10.

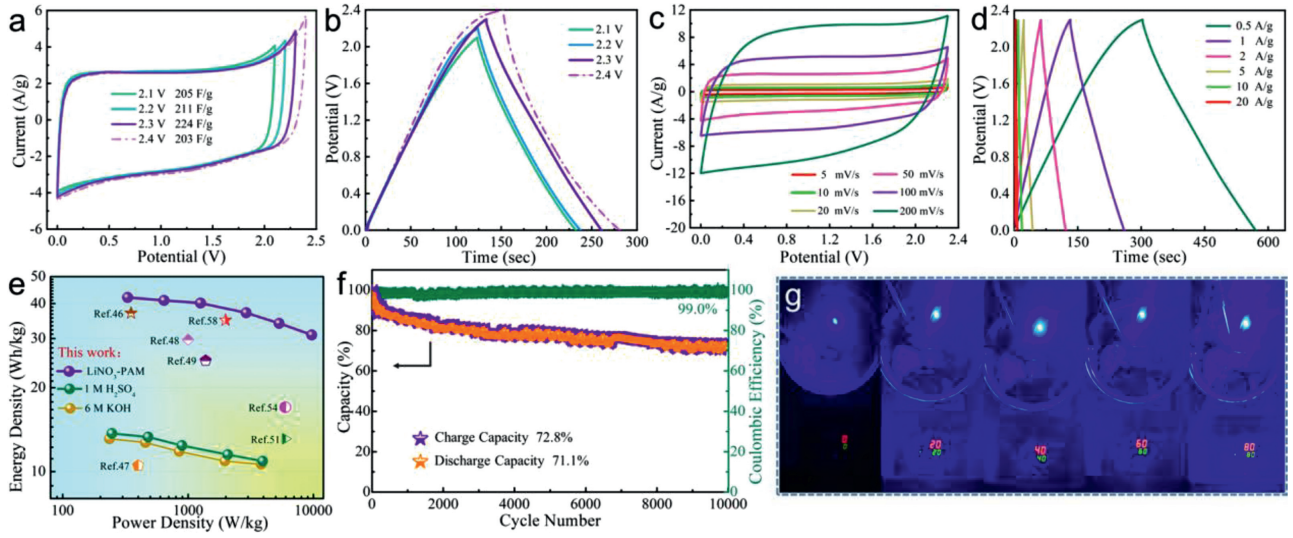

Fig. 6. Electrochemical performances of the symmetric supercapacitors based on CQA10 electrode using $LiNO_3$-PAM electrolyte: (a) CV curves at 10 mV/s under different potentials. (b) GCD curves at 1 A/g under different potentials. (c) CV curves. (d) GCD curves. (e) Ragone plots. (f) Cycling stability and coulombic efficiency. (g) The photographs of a lighted LED under temperatures ranging from 0 °C to 80 °C.

obtain improved energy densities and additional features such as stretchability and wearability [49,50]. Moreover, polymer electrolytes loaded with highly-concentrated salt solutions are considered to be ideal electrolytes but have been rarely reported [51]. Polyacrylamide (PAM) has a property of ultra-absorbing as a polymer, owing to the osmotic pressure difference caused by ionic groups inside and outside the gel network [52]. We find that $LiNO_3$ has a higher solubility of 6.9 g/10 mL than that of $Li_2SO_4{\cdot}H_2O$ (3.5 g/10 mL) at 22 °C which can be expected to effectively improve both ionic conductivity and electrochemical performance. Herein, we develop highly-concentrated $LiNO_3$-loaded polymer electrolytes with a wide voltage window in supercapacitor device, of which PAM is selected as the main polymer. For previous studies of Li_2SO_4-PAM polymer electrolytes endowed the activated carbon electrode with a stable 2.2 V performance, we conduct a full-scale tentative experiment for 2.1 V to 2.4 V voltage windows for symmetric supercapacitors [53]. Apart from the approximately rectangular shapes of CV curves corresponds to distinctive characteristic of EDLC, the 2.3 V based device exhibits an undistorted maximum voltage (Figs. 6a and c). By calculating the CV curves, capacitances at 10 mV/s in the descending sequence are 224 F/g (2.3 V) > 211 F/g (2.2 V) > 205 F/g (2.1 V) > 203 F/g (2.4 V) respectively, exceeding the capacitances exhibited by many neutral electrolytes [54,55]. At the comparative GCD test, within a 2.1–2.4 V voltage range, the charge–discharge plots are highly symmetrical, testifying a reversible ion adsorption/desorption procedure at the surface of CQA10 carbon. (Figs. 6b and d). Besides, the measured ionic conductivity of $LiNO_3$-PAM electrolyte has also been directly increased to 5.05 mS/cm [53]. A superb capacitance of 229 F/g achieves under a scan rate of 5 mV/s, together with maintained value of 168 F/g under a high scan rate of 200 mV/s (74.3% capacitance retention), displaying a good rate capability (Fig. 6c). In the EIS test, due to the high concentration conditions will induce the formation of extensive aggregation, the R_s and R_{ct} values are slightly high of 3.6 and 4.2 Ω, respectively (Fig. S11 in Supporting information) [56]. Benefiting from the greatly extended potential windows, $LiNO_3$-PAM polymer electrolyte and 1 mol/L $TEMABF_4$/PC organic electrolyte based cells offer boosted energy densities of 41.1 and 61.3 Wh/kg, corresponding to the volumetric energy densities of 22.8 and 34.1 Wh/L (Fig. 6e and Fig. S12 in Supporting information) [21,57]. Besides, the Ragone plot further reveals considerable aqueous device energy densities of 13.1 Wh/kg and 13.7 Wh/kg at ~246 W/kg under KOH/H_2SO_4 electrolytes. In addition, after 10,000 successive cycles at 10 A/g, the discharge capacity of CQA10 in $LiNO_3$-PAM exhibits limited loss to 71.1% with 99.0% coulombic efficiency retaining (Fig. 6f). With operating temperature ranging from 0 °C to 80 °C, the assembled device has stably lighted up a light-emitting diode (LED, 2 V/150 mA) for about 10 min, revealing the broad temperature applicability (Fig. 6g) [58,59]. Overall, the CQA10-loaded devices achieve distinguished specific capacitance values comparing with relevant literatures (Table S3 in Supporting information). Considering the relationship between energy density and the square of voltage window, the development of $LiNO_3$-PAM electrolyte to improve the working voltage window marks a significant step towards high energy storage equipment [60,61].

In summary, the robust precursor-level functionalized porous carbons are successfully fabricated by *in-situ* activation of direct coupled quinone-amines, where the strength of carbon backbones is effectively consolidated by a pre-stabilization route. Originating from different durations of pre-stabilization, diverse carbon topographies are captured of which CQA10 possess well-preserved microsphere morphology with coarse surface. Moreover, the representative carbon exhibits a high sample yield (68.3%), a rich carbon/electrolyte interface (2269 m^2/g) as well as successfully fixed N content (8.86 wt%). As fabricated supercapacitor manifests 383 F/g at 10 mV/s using H_2SO_4 electrolyte, and energy density of 41.1 Wh/kg at 643.4 W/kg employing $LiNO_3$-PAM polymer electrolyte. After 10,000 times of charge/discharge, the polymer device shows a high discharge performance of 71.1% and super coulombic efficiency of 99.0%.

Declaration of competing interest

The authors report no declarations of interest.

Acknowledgments

This work is financially supported by the National Natural Science Foundation of China (Nos. 21875165, 51772216, 21905207 and 22172111), the Science and Technology Commission of Shanghai Municipality, China (Nos. 20ZR1460300, 19DZ2271500 and 22ZR1464100), Zhejiang Provincial Natural Science Foundation of China (No. LY19B010003), the Fundamental Research Funds for the Central Universities, and the Large Equipment Test Foundation of Tongji University.

Supplementary materials

Supplementary material associated with this article can be found, in the online version, at doi:10.1016/j.cclet.2022.03.027.

References

[1] P. Simon, Y. Gogotsi, Nat. Mater. 19 (2020) 1151–1163.
[2] Y. Wang, R. Liu, Y. Tian, et al., Chem. Eng. J. 384 (2020) 123263.
[3] Y. Wang, Q. Qu, S. Gao, et al., Carbon 155 (2019) 706–726.
[4] Q. Yu, J. Lv, Z. Liu, et al., Sci. Bull. 64 (2019) 1617–1624.
[5] K. Jayaramulu, M. Horn, A. Schneemann, et al., Adv. Mater. 33 (2021) 2004560.
[6] J. Yin, W. Zhang, N.A. Alhebshi, et al., Small Methods 4 (2020) 1900853.
[7] S. Li, J. Fu, G. Miao, et al., Adv. Mater. 33 (2021) 2008424.
[8] Z. Liu, Q. Yu, Y. Zhao, et al., Chem. Soc. Rev. 48 (2019) 285–309.
[9] X. Li, Z. Liu, C. Cai, et al., ChemSusChem 14 (2021) 1756–1762.
[10] S. Feng, Z. Liu, Q. Yu, et al., ACS. Appl. Mater. Interfaces 11 (2019) 4011–4016.
[11] J. Du, L. Liu, Y. Yu, et al., J. Mater. Chem. A 7 (2019) 1038–1044.
[12] M. Yu, R. Dong, X. Feng, J. Am. Chem. Soc. 142 (2020) 12903–12915.
[13] H. Xu, C. Wu, X. Wei, et al., J. Mater. Chem. A 6 (2018) 15340–15347.
[14] L. Miao, H. Duan, D. Zhu, et al., J. Mater. Chem. A 9 (2021) 2714–2724.
[15] T. Shiga, R. Kumamaru, G.N. Newton, et al., Dalton Trans. 49 (2020) 1485–1491.
[16] F.L. Zeng, X.L. Chen, S.Q. He, et al., Org. Chem. Front. 6 (2019) 1476–1480.
[17] Q.Z. Zhong, J.J. Richardson, A. He, et al., Angew. Chem. Int. Ed. 60 (2021) 2346–2354.
[18] S. Lisboa Cda, V.G. Santos, B.G. Vaz, et al., J. Org. Chem. 76 (2011) 5264–5273.
[19] W. Mao, W. Yue, Z. Xu, et al., ACS Nano 14 (2020) 4741–4754.
[20] Z.A. Lan, G. Zhang, X. Chen, et al., Angew. Chem. Int. Ed. 58 (2019) 10236–10240.
[21] M. Xie, H. Meng, J. Chen, et al., ACS Appl. Energy Mater. 4 (2021) 1840–1850.
[22] J. Kim, J.H. Jeong, H.J. Ahn, et al., ChemElectroChem 7 (2020) 2410–2417.
[23] X. Hu, Y. Wang, B. Ding, et al., J. Alloys Compd. 785 (2019) 110–116.
[24] Y. Li, Y. Liang, H. Hu, et al., Carbon 152 (2019) 120–127.
[25] Y. Tian, C. Xiao, J. Yin, et al., ChemistrySelect 4 (2019) 2314–2319.
[26] D. Yu, C. Chen, G. Zhao, et al., ChemSusChem 11 (2018) 1678–1685.
[27] W.J. Liu, H. Jiang, H.Q. Yu, Energy Environ. Sci. 12 (2019) 1751–1779.
[28] C. Ma, X. Chen, D. Long, et al., Carbon 118 (2017) 699–708.
[29] S. Kang, S. Park, K.S. Kim, et al., J. Org. Chem. 83 (2018) 2694–2705.
[30] C. Ibis, A.F. Tuyun, Z. Ozsoy-Gunes, et al., Eur J. Med. Chem. 46 (2011) 5861–5867.
[31] F. Xu, S. Yang, X. Chen, et al., Chem. Sci. 10 (2019) 6001–6006.
[32] D. Fang, B. Yan, S. Agarwal, et al., J. Mater. Sci. 56 (2021) 9344–9355.
[33] Y. Sun, P. Lu, X. Liang, et al., J. Alloys Compd. 786 (2019) 468–474.
[34] S. Lee, J.-S. Kang, K.T. Leung, et al., Appl. Surf. Sci. 386 (2016) 393–404.
[35] Z. Zhou, L. Miao, H. Duan, et al., Chin. Chem. Lett. 31 (2020) 1226–1230.
[36] Y. Wang, X. Lin, T. Liu, et al., Adv. Funct. Mater. 28 (2018) 1806207.
[37] G. Lin, R. Ma, Y. Zhou, et al., Electrochim. Acta 261 (2018) 49–57.
[38] J. Du, L. Liu, Z. Hu, et al., ACS Sustainable Chem. Eng. 6 (2018) 4008–4015.
[39] D. Li, X. Ren, Q. Ai, et al., Adv. Energy Mater. 8 (2018) 1802386.
[40] G. Ping, L. Miao, A. Awati, et al., Chin. Chem. Lett. 32 (2021) 3811–3816.
[41] J. Li, N. Wang, J. Tian, et al., Adv. Funct. Mater. 28 (2018) 1806153.
[42] W. Dong, Z. Wang, Q. Zhang, et al., J. Power Sources 419 (2019) 137–147.
[43] G. Li, Y. Li, J. Deng, et al., Mater. Chem. Front. 4 (2020) 2704–2715.
[44] Y. Yan, Y.S. He, X. Zhao, et al., Nano Energy 84 (2021) 105935.
[45] T. Liu, Z. Zhou, Y. Guo, et al., Nat. Commun. 10 (2019) 675.
[46] Y. Chen, J. Zhu, N. Wang, et al., J. Mater. Chem. A 9 (2021) 7005–7017.
[47] C. Wang, X. Li, W. Yang, et al., Chin. Chem. Lett. 32 (2021) 2909–2913.
[48] L. Suo, O. Borodin, Y. Wang, et al., Adv. Energy Mater. 7 (2017) 1701189.
[49] S.W. Zhang, B.S. Yin, X.X. Liu, et al., Nano Energy 59 (2019) 41–49.
[50] X. Zhao, Y. Wang, Y. Shi, et al., ACS Energy Lett. 6 (2021) 1134–1140.
[51] J. Jiang, B. Liu, G. Liu, et al., Electrochim. Acta 274 (2018) 121–130.
[52] M. Shi, W. Yang, Z. Zhang, et al., J. Mater. Chem. A 10 (2022) 2966–2972.
[53] A. Virya, K. Lian, Electrochem. Commun. 81 (2017) 52–55.
[54] F. Ran, X. Yang, X. Xu, et al., Chem. Eng. J. 412 (2021) 128673.
[55] H. Luo, Y. Yang, B. Mu, et al., Carbon 100 (2016) 214–222.
[56] Z. Song, L. Miao, L. Ruhlmann, et al., Adv. Mater. 33 (2021) 2104148.
[57] S. Feng, Z. Liu, Q. Yu, et al., ACS Appl. Mater. Interfaces 11 (2019) 4011–4016.
[58] M. Xu, Y. Liu, Q. Yu, et al., Chin. Chem. Lett. 32 (2021) 184–189.
[59] X. Zheng, L. Miao, Z. Song, et al., J. Mater. Chem. A 10 (2022) 611–621.
[60] Y. Zhang, J. Li, W. Zhao, et al., Adv. Mater. 34 (2022) 2108114.
[61] L. Zhou, Z. Zhuang, H. Zhao, et al., Adv. Mater. 29 (2017) 1602914.